Electrophysiology Catheter Detection and Reconstruction from Two Views in Fluoroscopic Images

Matthias Hoffmann, Alexander Brost, Martin Koch, Felix Bourier, Andreas Maier, Klaus Kurzidim, Norbert Strobel and Joachim Hornegger

***Abstract*—Electrophysiology (EP) studies and catheter ablation have become important treatment options for several types of cardiac arrhythmias. We present a novel image-based approach for automatic detection and 3-D reconstruction of EP catheters where the physician marks the catheter to be reconstructed by a single click in each image. The result can be used to provide 3-D information for enhanced navigation throughout EP procedures. Our approach involves two X-ray projections acquired from different angles, and it is based on two steps: First, we detect the catheter in each view after manual initialization using a graph-search method. Then, the detection results are used to reconstruct a full 3-D model of the catheter based on automatically determined point pairs for triangulation. An evaluation on 176 different clinical fluoroscopic images yielded a detection rate of 83.4 %. For measuring the error, we used the coupling distance which is a more accurate quality measure than the average point-wise distance to a reference. For successful outcomes, the 2-D detection error was 1.7 mm ± 1.2 mm. Using successfully detected catheters for reconstruction, we obtained a reconstruction error of 1.8 mm ± 1.1 mm on phantom data. On clinical data, our method yielded a reconstruction error of 2.2 mm ± 2.2 mm.**

***Index Terms*—Detection, Reconstruction, Catheters, Fluoroscopy, Ablation, Electrophysiology.**

I. Introduction

CATHETER ablation is a minimally invasive treatment option for several types of heart arrhythmia, e.g. for paroxysmal atrial fibrillation (AFib). The standard treatment option for paroxysmal AFib is electrical isolation of the pulmonary veins [1]. This often involves a radio frequency (RF) ablation catheter to generate lesions around the pulmonary vein (PV) ostia. In addition, a circular mapping (CM) catheter is generally used to monitor the electrical signals at the ostium of each PV. Finally, a coronary sinus (CS) catheter is usually placed in the coronary sinus vein to facilitate pacing when required. Navigation during EP procedures can either be performed under X-ray or using electro-anatomical mapping systems [2], [3]. X-ray provides the physician with a real-time image at a high spatial resolution as shown in Fig. 1. The disadvantage of X-ray imaging is its low soft tissue contrast, e.g. a chamber such as the left atrium is only visible when contrast is injected. Furthermore, fluoroscopic images provide no depth information. As a consequence, the exact 3-D shape and position of catheters have to be figured out mentally. A biplane fluoroscopic system simplifies navigation as X-ray imaging can easily be carried out from two different, usually orthogonal, viewing directions, if required even at the same time.

If we adopt X-ray images as our view on a patient, augmented reality concepts can be applied to enhance navigation during interventional procedures. For example, 3-D objects

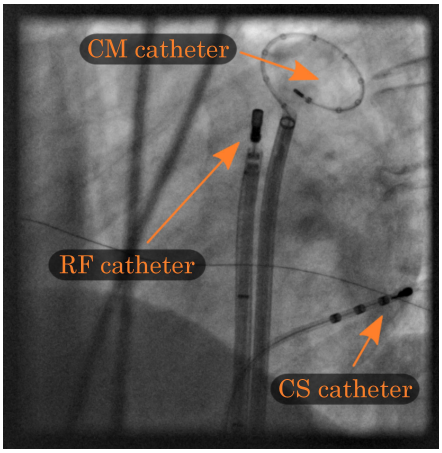

Fig. 1. Common catheters used for electrophysiology (EP) procedures. A radio-frequency (RF) ablation catheter is used to generate lesions inside the left atrium, the circular mapping catheter (CM) records electrograms inside the heart, and the coronary sinus (CS) catheter is used for pacing.

This work was supported by the German Federal Ministry of Education and Research (BMBF) in the context of the initiative Spitzencluster Medical Valley - Europäische Metropolregion Nürnberg, project grant Nos. 12EX1012A and 12EX1012E, respectively. Additional funding was provided by Siemens Healthcare GmbH. J. Hornegger and A. Maier gratefully acknowledges funding of the Erlangen Graduate School in Advanced Optical Technologies (SAOT) by the German Research Foundation (DFG) in the framework of the German excellence initiative. The concepts and information presented in this paper are based on research and are not commercially available.

M. Hoffmann, M. Koch, A. Maier and J. Hornegger are with Pattern Recognition Lab, Friedrich-Alexander-Universität Erlangen-Nürnberg, 91058 Erlangen, Germany, e-mail: Matthias.Hoffmann@cs.fau.de

F. Bourier is with Department of Electrophysiology, German Heart Center Munich, Technische Universität Munich, 80636 Munich, Germany

K. Kurzidim is with Klinik für Herzrhythmusstörungen, Krankenhaus Barmherzige Brüder, 93049 Regensburg, Germany

A. Brost and N. Strobel are with Siemens Healthcare GmbH, 91301 Forchheim, Germany

J. Hornegger is with Erlangen Graduate School in Advanced Optical Technologies (SAOT), 91052 Erlangen, Germany

which are registered to the X-ray images can be fused with the live fluoroscopic images using overlay techniques [4]. A typical example is a 3-D model of the patient heart segmented, e.g., from voxel data acquired using computed tomography or magnetic resonance imaging. Besides 3-D anatomical information, other graphical objects or additional text can be added. As of today, manual triangulation of the catheter is required to visualize the 3-D shape of a catheter with respect to a registered heart model. This can be a time consuming task, and we developed a method for catheter detection and reconstruction which requires considerable less user interaction.

The long term success of a RF ablation depends on the catheter tip-to-heart wall contact force [5]. Recent studies have shown that the contact force can be computed if the catheter bending is known [6]. A 3-D catheter model, generated using our proposed technique, could be used as input for this bending-based force estimation method.

A. Previous Work

A combined approach for detection and reconstruction of catheters was presented by Bender *et al.* [7]. This approach was designed to verify catheter placement in intensive care patients under X-ray. The assumptions made, e.g., low catheter curvature, do, however, not meet EP requirements. Franken *et al.* proposed a method for EP catheter detection [8]. The main focus was placed on automatic catheter tip detection. When trying to extend their algorithm to the detection of the full catheter, the success rate was found to be low. Another approach for catheter tip detection was presented by Yatziv *et al.*, [9]. This approach cannot be applied to single images as it requires image sequences to compute a mean image representing the background. From this background image, an image from the sequence is subtracted to obtain moving structures such as catheters including their shafts. Starting from a point marked by the user, potential catheter shafts are traced. However, this information is not processed further in order to detect the complete catheter shafts, but rather used to reduce the search space for catheter tips. Another catheter tip detection method based on blob detection was presented by Ma *et al.* [10]. An alternative detection method is the fusion of hypotheses generated by a number of learning-based detectors in a Bayesian framework [11]. Both methods focus on electrodes only, thus, limiting catheter reconstruction to those catheter segments that carry electrodes. As a consequence, detection of catheters not carrying electrodes, such as the cryoballoon catheter, is not possible. Another detection approach was presented by Cazalas *et al.* [12], and an approach with focus on overlapping catheters was presented by Milletari *et al.* [13]. Again, these approaches detect only catheter tips and not the whole catheter. Without detection and 3-D reconstruction of the full catheter, little information about the overall catheter shape can be provided. This information is important to, e.g., assess a catheter's fit to the anatomy at hand.

A method to detect curvilinear structures in fluoroscopic images was presented by Wang *et al.* [14]. They proposed a graph-based approach which requires the user to mark the start and the end point of the object. Additional points can be manually added to increase the accuracy of the method. Although the method can be adapted to EP catheters, it has only been evaluated for guide wires.

Previous work on guide wire detection [15], [16], [17], [18] cannot be applied to catheters directly either. In X-ray images, guide wires present themselves as thin, homogeneously dense objects with little variance in appearance. Catheters, however, can vary in thickness, e.g. if they are located inside a sheath. They also differ in contrast, especially in the regions around the electrodes.

Tracking of catheters is related to catheter detection, but it requires prior information, such as an initialization at the beginning or the result of a previous frame. If a 3-D structure is tracked using images from different views, it is also related to reconstruction. Tracking of EP catheters in 3-D can be performed by altering the 3-D structure until its projections fit the 2-D images [19], [20] or by 2-D tracking in both fluoroscopic images followed by a calculation of the 3-D position based on the 2-D objects. This approach was used by Baert *et al.* [21] for tracking of guide wires with low curvature. So far, only Brost *et al.* [22] focused on curved objects, but their approach is limited to the elliptical part of the CM catheter.

B. Contribution and Outline

We propose a novel method to detect and reconstruct complete EP catheters from two different views which runs automatically after manual initialization. In contrast to [9], it requires only a single image per view rather than a sequence and can accommodate, unlike the methods in [7], [21], highly curved objects such as the CM catheter. Our proposed method reduces the required manual interaction to a single click in each image plane for each catheter, and it can be seamlessly integrated into the workflow of typical EP procedures. The resulting 3-D catheter model can be used for 3-D visualization of anatomical landmarks [23] or for documentation of a static scene during the procedure or retrospectively after the procedure. If dynamic visualization is required, the method can be used to calculate the initialization for catheter tracking [20]. Recently, a method for initial registration of a 3-D patient heart model was proposed [22]. This method would be performed only a few times during the procedure and requires as input the 3-D shape of the CS catheter, which also can be obtained using our proposed method. Furthermore, the method can compute the 3-D shape of a RF catheter which can be used for estimating its contact force [6]. Our previous approach [24], [25] was designed for CM catheter detection. We extended this approach by introducing a learning-based framework that allows the method to adapt to arbitrary line-shaped catheters in a training step. In this context, the constraint on the catheter curvature was changed to adapt to more bent catheters such as the CS catheter. Furthermore, we performed a comprehensive evaluation of the detection and the reconstruction step as well as their combination both on phantom data as well as on a large clinical data set. In addition to our previous publication, we

perform an evaluation with respect to the coupling error [26] which allows a better judgement of the detection results, but we use also the distance of the detection result to a reference to maintain comparability.

This paper is structured as follows. In Section II, we provide details on our catheter detection. Catheter reconstruction is explained in Section II-D. Evaluation results are presented in Section III, and we discuss our findings in Section IV. Finally, we draw conclusions from our work in Section V.

II. Catheter Detection and Reconstruction

Our catheter detection and reconstruction algorithm comprises four steps. After manually placing a seed point on the catheter, the image is filtered to enhance catheter-like structures as a first step. In addition, the search space is reduced to catheter-like structures that are close to the seed point. In the second step, candidates for catheter segments are identified and organized in a graph structure. In the third step, combinations of different catheter segments are evaluated using features that are selected with respect to certain catheter properties. An evolutionary algorithm is used to search for a combination of catheter segments that fits best to these defined properties. After catheter detection in two views, 3-D catheter reconstruction is performed as a last step. These steps are explained in detail below.

A. Search Space Reduction

At first, a seed point $\boldsymbol{s} \in \mathbb{N}^2$ is manually placed on the catheter depicted in a digital X-ray image. For linear catheters such as the ablation catheter and the CS catheter, the seed point has to be put on the tip electrode. For the circular mapping catheter, the seed point needs to be placed shortly after the position where the shaft connects to the elliptical part of the CM catheter. Afterwards, the image is filtered using a medialness filter [27], see Fig. 2(b). In the filtered output, catheter-like structures are enhanced, while other structures are supressed. This image is denoted by $\boldsymbol{I}_\mathrm{f}$, $\boldsymbol{I}_\mathrm{f}(i,j) \in \{0,\dots,\boldsymbol{I}_\mathrm{f}^\mathrm{max}\}$. Without loss of generality, we normalize $\boldsymbol{I}_\mathrm{f}$ such that $\boldsymbol{I}_\mathrm{f}^\mathrm{max} = 255$. After image filtering, a binary image is generated using a *variable threshold* [28]. To reduce noise, especially in the area close to the catheter and to close holes within the catheter, an additional opening and closing is performed on the binarization. The resulting image is denoted by $\boldsymbol{I}_\mathrm{b}$. Afterwards, a skeleton $\boldsymbol{I}_\mathrm{s}$ of the catheter is computed [29], as shown in Fig. 2(c), and the seed point is moved to the nearest skeleton point.

Next, we identify those pixels that belong to the catheter. The goal is to obtain a reduced search space $\mathcal{S}_\mathrm{r}$ containing the complete catheter and as few background pixels as possible. Simply using the skeleton pixels connected to the seed point is not sufficient as the skeleton along the catheter may contain gaps. To handle these gaps, we define a cost $c_\mathrm{r}(\boldsymbol{p})$ for each pixel $\boldsymbol{p} = (i,j)^T$ and compute the set $\mathcal{S}_\mathrm{r}$ of pixels in the original image that are closest to the seed point with respect to this cost. This is done using Dijkstras' algorithm [30]. To apply it, we consider the images as a graph where each pixel represents a node that is connected to its four neighbours by an edge. The cost of the edge depends solely on the target pixel $\boldsymbol{p}$ and is defined by

$$c_\mathrm{r}(\boldsymbol{p}) = \begin{cases} 1 & \text{if } \boldsymbol{I}_\mathrm{s}(\boldsymbol{p}) = 1 \\ \min\left(\boldsymbol{I}_\mathrm{f}^\mathrm{max} - \boldsymbol{I}_\mathrm{f}(\boldsymbol{p}), \lambda\|\boldsymbol{p}-\boldsymbol{s}\|_2\right) & \text{if } \boldsymbol{I}_\mathrm{b}(\boldsymbol{p}) = 1 \\ \boldsymbol{I}_\mathrm{f}^\mathrm{max} - \boldsymbol{I}_\mathrm{f}(\boldsymbol{p}) & \text{otherwise} \end{cases} \tag{1}$$

Pixels on the skeleton $\boldsymbol{I}_\mathrm{s}$ have a low cost since the skeleton outlines catheters very well. To handle gaps in the skeleton, the cost of the other pixels is determined by the filter value such that a high filter value corresponds to a low cost. Especially around the electrodes, the CM catheter may have a low contrast which can result in several small patches in the binarized image $\boldsymbol{I}_\mathrm{b}$ that are separated by little gaps. During skeletonization, a small patch may shrink to a single point with a large gap to the next skeleton part. To ensure that the catheter tip is completely included in the search space, pixels that occur in the binarization $\boldsymbol{I}_\mathrm{b}$ and are located close to the seed point $\boldsymbol{s}$ receive special treatment in Eq. 1. The impact of the proximity to $\boldsymbol{s}$ is governed by a weighting factor λ that sets the size of the CM catheter tip in relation to $\boldsymbol{I}_\mathrm{f}^\mathrm{max}$. Dijkstras algorithm is terminated when the desired search space size $|\mathcal{S}_\mathrm{r}|$ is reached. The size $|\mathcal{S}_\mathrm{r}|$ should be chosen according to the expected number of pixels covered by the catheter in the image.

B. Search Graph Generation

In the previous step, we restricted our search space to the pixels in $\mathcal{S}_\mathrm{r}$. Pixels of the image which are both part of the skeleton and elements of $\mathcal{S}_\mathrm{r}$ form potential catheter segments. The goal of this second step is to extract these segments from $\mathcal{S}_\mathrm{r}$ and to organize them in a graph structure which is illustrated by Fig. 2(e). The edges of this graph represent the segments. Connections between the segments are modelled as nodes.

The transformation to the graph representation cannot be performed solely based on the skeleton, because it is not necessarily continuously connected. Therefore we impose a graph structure on all pixels in $\mathcal{S}_\mathrm{r}$. This graph is a tree, which has $\boldsymbol{s}$ as root and the main branches of the tree follow the skeleton. Every pixel becomes a graph node and is connected by an edge to a neighboring pixel. In a first step, relevant endpoints, so called feature points, are determined and only the paths from these feature points to the root are retained in the graph.

1) Tree Generation: In the beginning, the graph consists of all pixel in $\mathcal{S}_\mathrm{r}$ which are 4-connected. The tree is computed as a shortest path tree using again Dijkstras' algorithm with $\boldsymbol{s}$ as start. For the cost function, a distance transform [31] $\boldsymbol{I}_{DT}$ of the skeleton is computed. $\boldsymbol{I}_{DT}(i,j)$ is the Euclidean distance to the next skeleton pixel. The cost $c_\mathrm{f}(\boldsymbol{p})$ for each pixel $\boldsymbol{p}$ is defined by

$$c_\mathrm{f}(\boldsymbol{p}) = \begin{cases} \infty & \boldsymbol{p} \notin \mathcal{S}_\mathrm{r} \\ (\boldsymbol{I}_\mathrm{f}^\mathrm{max} - \boldsymbol{I}_\mathrm{f}(\boldsymbol{p})) \cdot \min\left(\frac{\boldsymbol{I}_{DT}(\boldsymbol{p})+1}{\varrho}, 1\right) & \text{otherwise.} \end{cases} \tag{2}$$

The distance from a pixel $\boldsymbol{p}$ to $\boldsymbol{s}$ with respect to this cost is denoted by $\delta_{\boldsymbol{s}}(\boldsymbol{p})$. In Eq. (2), we combine the filtered image

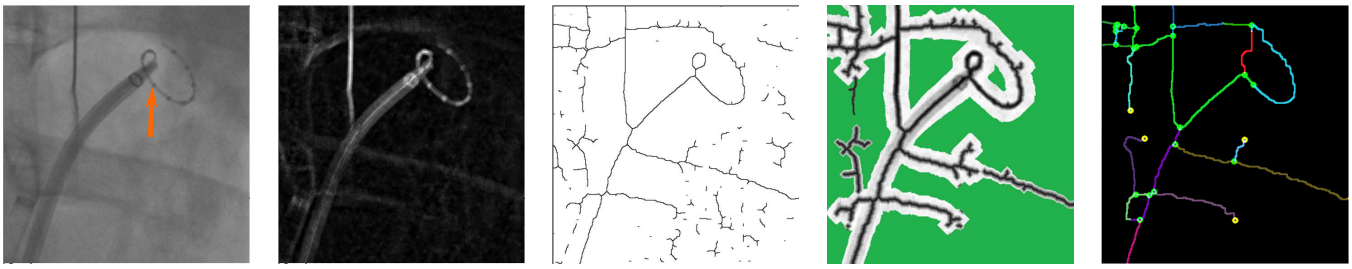

(a) (b) (c) (d) (e)

Fig. 2. Catheter detection involves several steps. After placing a seed point in the the original image (a), a medialness filter is applied (b). Using a variable threshold, a binary image and then a skeleton image (c) is computed. Using the medialness filtered image and the skeleton, the search space is reduced and a cost c_f for each pixel is defined (d); green pixels are outside the search space $\mathcal{S}_\mathrm{r}$ and their cost is set to infinity. Based on this cost, the shortest path from each pixel to the seed point is computed. Finally, feature points such as endpoints of the skeleton are selected. Their shortest paths to the seed point are used to transform the skeleton into a graph (e). For illustration, each path from a feature point to a node is given a different color to make them easily distinguishable. Starting from the seed point which is marked in (a) with an arrow, a path in this graph is searched that fits best to a set of predefined features.

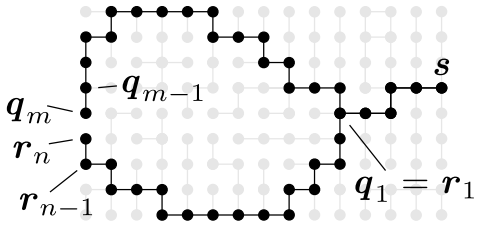

Fig. 3. Schematic drawing of the tree with the seed point $\boldsymbol{s}$ as root. Circles in the skeleton (black) can be found by considering pixels at which two paths from different directions meet. For a circle, the first feature point, $\boldsymbol{q}_m$, is a point on the skeleton that has a higher distance $\delta_{\boldsymbol{s}}$ to the seed point than its neighboring points on the skeleton. As $\boldsymbol{q}_{m-1}$ is on the path from $\boldsymbol{q}_m$ to $\boldsymbol{s}$, the neighbor $\boldsymbol{r}_n$ has to be the other feature point. The paths $\boldsymbol{q}_1 \to \ldots \to \boldsymbol{q}_m$ and $\boldsymbol{r}_n \to \ldots \to \boldsymbol{r}_1 = \boldsymbol{q}_1$ will be merged after computing all feature points.

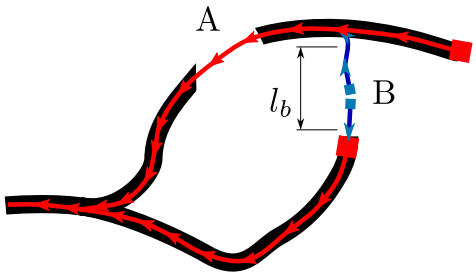

Fig. 4. The skeleton (black line) may contain gaps. The graph creation is robust w.r.t. gaps (A) between skeleton endpoints and the seed point as they are bridged by the shortest paths from the endpoints (red squares). The same holds for gaps in a circle unless the feature points forming the circle fall into these gaps (B). For such a case, additional bridges (blue) are computed that connect parts of the graph that are not connected by the skeleton.

and the skeleton image. An example of this cost function is shown in Fig. 2(d). The main branches of the shortest path tree should be smooth and follow the skeleton as closely as possible. Therefore, within a range of ϱ pixels around the skeleton, the cost is decreased depending on the distance to the skeleton given by $\boldsymbol{I}_{DT}$. The value of ϱ depends on the smoothness of the skeleton and is typically a number between 5 and 10.

Also within the ϱ-pixel range, the values of $\boldsymbol{I}_\mathrm{f}$ are important. Without these values, the distance measure would degenerate to a Euclidean metric. This will be more important for the shaft search presented later in Section II-C1: In rare cases, such a degenerated distance measure might result in favoring a shorter connection instead of a longer path which might present a better filter response.

2) Feature Points: The first and second set of feature points are based on the skeleton. Therefore we process only skeleton pixels in these stages. The first set consists of pairs of neighboring pixels $\boldsymbol{q}_m, \boldsymbol{r}_n$ with partially different shortest paths to the seed point that describe a circle. The paths are denoted by

$$(\boldsymbol{q}_m \to \boldsymbol{q}_{m-1} \to \ldots \to \boldsymbol{q}_1 \to \ldots \to \boldsymbol{s}) \text{ and}$$
$$(\boldsymbol{r}_n \to \boldsymbol{r}_{n-1} \to \ldots \to \boldsymbol{r}_1 \to \ldots \to \boldsymbol{s}) \text{ with } \boldsymbol{q}_1 = \boldsymbol{r}_1.$$

So, they describe a circle

$$(\boldsymbol{q}_1 \to \ldots \to \boldsymbol{q}_m \to \boldsymbol{r}_n \to \ldots \to \boldsymbol{r}_1 = \boldsymbol{q}_1)$$

in the image, see Fig. 3. Assuming, $\delta_{\boldsymbol{s}}(\boldsymbol{q}_m) \geq \delta_{\boldsymbol{s}}(\boldsymbol{r}_n)$, $\boldsymbol{q}_m$ can be found by searching for skeleton pixels that have a higher $\delta_{\boldsymbol{s}}$ value than their neighbors. The neighboring pixel that follows $\boldsymbol{q}_m$ on the shortest path to $\boldsymbol{s}$ is $\boldsymbol{q}_{m-1}$, the other neighbor is $\boldsymbol{r}_n$. The length l_c is given by $(m+n-1)$ as the start pixel of the circle is contained in both paths. Pairs with a l_c below a certain threshold are not considered as feature points.

The second set of feature points are the endpoints of the skeleton. They are defined as points on the skeleton that have only one neighbour on the skeleton. Then, from the original tree, a simplified graph is created that contains only edges and nodes that are part of a path from a feature point to the seed point. Nodes with two adjacent edges are removed and the two edges are merged.

The resulting graph might lack some relevant edges due to the non-contiguous skeleton. To close remaining gaps, we look for neighboring, unconnected nodes of the original tree such that their shortest path connects two existing edges, see Fig. 4. The detection of missing connections is similar to the detection of circle feature points. In this case, however, not only skeleton pixels, but all pixels in the search space $\mathcal{S}_\mathrm{r}$ computed in Section II-A are considered. Every pixel $\boldsymbol{p}$

is tested if its δ_s distance is higher compared to all of its neighboring pixels. In this case, for each pair formed by $\boldsymbol{p}$ and a neighboring pixel, the shortest paths from the two pixels to the seed point will be evaluated. The value l_b is computed as the number of pixels in both paths that are not yet part of the simplified graph, and l_c is computed as above for the circles on the skeleton. If l_c and the fraction l_c/l_b is larger than a certain threshold, these paths will be added to the simplified graph. If there exist several pairs of feature points whose paths connect to the same edges, only the connection with the highest ratio l_c/l_b will be added.

Finally, adjacent unconnected nodes are connected by an edge to introduce circles. Stubs, i.e. short edges leading to a leave node with a length below a certain threshold, are removed.

C. Catheter Search

The computed graph defines the catheter search space. The search for the catheter is constrained by the information provided by the seed point. We differentiate two types of catheter detections. Linear catheters, such as the RF and the CS catheters, only require a search for the shaft, while the circular mapping catheter also requires a search for its elliptical upper part, denoted as 'tip' or 'tip section', respectively.

1) Shaft Search: For standard C-arm view directions, prior knowledge about the image content can be taken into account. In our cases, where catheters are inserted at the groin area, the catheter shafts enter the image from the bottom. As a consequence, all pixel sequences forming shortest paths on the graph from the seed point to nodes of the graph located in the lower 60% of the image are considered as shaft candidates. The shortest paths are defined by the cost function given in Eq. (2). The number of different shortest paths depends on the image. For noisy images where many other linear structures such as ECG-leads or other catheters cross, we may end up with several, partially overlapping paths, e.g., up to 20. For images with low noise where no other structure crosses the catheter, there may be only one or two shortest paths. The catheter does, however, not need to be identical to the complete pixel sequence given by a shortest path which may comprise additional pixels that reach beyond the actual catheter. Therefore, an evaluation is performed not only on the complete pixel sequence, but also on sub-sequences $\mathcal{F}$ which start at the seed point and have increasing sizes. Ideally, one would increase the path pixel by pixel, but this increases the number of paths that have to be evaluated. If, on the other hand, the path is increased by a large number of pixels, then either a large part of the catheter end section may be left out or too many pixels not belonging to the catheter may be included. In our case, we settled on a length for the first sub-sequence $\mathcal{F} = [\boldsymbol{p}_1, \ldots, \boldsymbol{p}_{|\mathcal{F}|}]$ of 100 pixels, and each subsequent fraction is increased by 30 pixels. This turned out to be a good trade-off between performance and accuracy. A visualization of all resulting subsequences $\mathcal{F}$ formed this way is given in Fig. 5.

The following features of a subsequence $\mathcal{F}$ are taken into account by the optimization step:

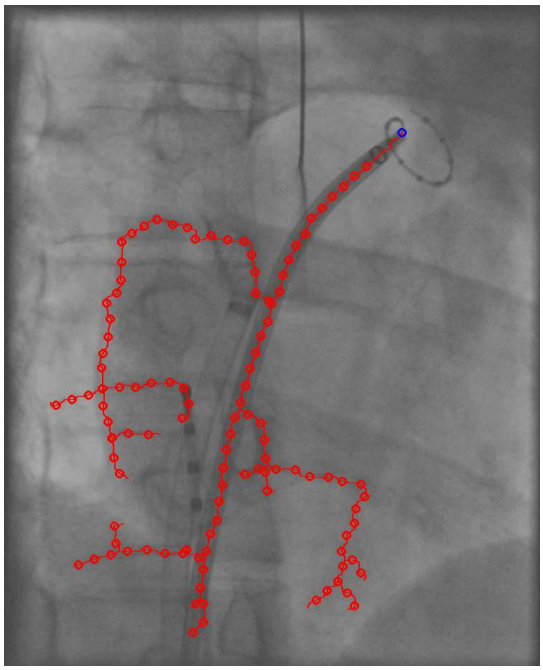

Fig. 5. All paths from the seed point (blue circle) to graph nodes in the lower part are used to determine shaft candidates. These paths are not evaluated as a whole, but subsequences $\mathcal{F}$ of increasing length are formed. While all of them have a common start point (blue circle), their respective endpoint (denoted by a red circle) is different.

- The length $|\mathcal{F}|$ of the subsequence, as the catheter should be as complete as possible.
- The mean squared value a_c of the curvature. It is given by

$$a_c(\mathcal{F}) = \frac{1}{|\mathcal{F}|} \sum_{t=1}^{|\mathcal{F}|} \kappa_{\mathcal{F}}(t)^2. \tag{3}$$

  The curvature of the sequence at pixel $\boldsymbol{p}_t$ is denoted by $\kappa_{\mathcal{F}}(t)$. By using the squared value, high curvature values are penalized more strongly. This favors low curvatures which are more common for linear catheters.
- The integral a_d of the deviation of the path from $-90°$

$$a_d(\mathcal{F}) = \sum_{t=1}^{|\mathcal{F}|} \left| \phi_{\mathcal{F}}(t) - \frac{-\pi}{2} \right| \tag{4}$$

  where the angle $\phi_{\mathcal{F}}(t)$ denotes the angle of the tangent to the pixel sequence at pixel $\boldsymbol{p}_t$. This feature applies to catheters inside the left atrium inserted via transseptal puncture. In this case, the overall direction of the shaft should be around $-90°$. For procedures where the catheters are aligned differently, this feature should be adapted or taken out.
- The angle a_a of the path at the bottom end. It is computed as

$$a_a(\mathcal{F}) = \left| \phi_{\mathcal{F}}(|\mathcal{F}|) - \frac{-\pi}{2} \right| \tag{5}$$

  By incorporating prior knowledge, we ensure that the detected catheters enter the image in an almost vertical direction, such that the direction of the shaft is close to $-90°$. The intention of this term is to determine a stopping

criterion for the path search. While the other features are global features for which changes at the end have lesser impact, this feature is focused on the end of the catheter. The decision whether to take a longer path depends highly on this feature. In the end, when the angle of the catheter approaches $-90°$, this term needs to be minimized and a longer path with a too strong deviation from this angle is not preferred to a shorter path with a better angle at the end. This way, a detection along a horizontal edge in the lower part of an X-ray image, e.g. introduced by a shutter, can be avoided.

Each feature is weighted with a corresponding factor α. Using a full search on all shaft candidates, the sub-sequence $\hat{p}$ that optimizes the objective function

$$\hat{p} = \arg\min_{\mathcal{F}}(-\alpha_l \cdot |\mathcal{F}| + \alpha_c \cdot a_c(\mathcal{F}) + \alpha_d \cdot a_d(\mathcal{F}) + \alpha_a \cdot a_a(\mathcal{F})) \quad (6)$$

is found. It is considered the best estimate for the catheter shaft. As only the length $|\mathcal{F}|$ needs to be maximized, α_l has a negative sign.

2) Tip Section Search: In contrast to the shaft search, no additional information about the orientation of the elliptical tip section of the CM catheter can be obtained from the seed point $\boldsymbol{s}$. Therefore all possible sequences that are not used for the shaft need to be considered as candidates for the tip section. Similar to the shaft search, the candidates for the tip are paths $\mathcal{G} = [\boldsymbol{p}_1 \dots \boldsymbol{p}_{|\mathcal{G}|}]$ which start at $\boldsymbol{s}$ and increase in length. Since the shape of the catheter is approximately circular, it resembles an ellipse when projected to 2-D. This strong characteristic is already used for tracking approaches [32], [33], [22]. For tip section detection, an ellipse is fitted to the points of the catheter tip candidate $\mathcal{G}$. The candidate is evaluated with respect to the quality of the ellipse fitting and the values of the medialness filtering $\boldsymbol{I}_\mathrm{f}$ along the fitted ellipse.

In a first step, six equidistant points are taken from the point sequence $\mathcal{G}$ to which an ellipse $\mathcal{E}(\mathcal{G})$ is fitted. The resulting ellipse is given by a set $\{\boldsymbol{e}_1 \dots \boldsymbol{e}_{|\mathcal{E}(\mathcal{G})|}\}$ of pixels $\boldsymbol{e}$ that are covered by the ellipse. In the next step, several features for the catheter tip section candidate $\mathcal{G}$ and its associated ellipse $\mathcal{E}$ are computed:

- The mean filter value b_fe of the ellipse is calculated as

$$b_\mathrm{fe} = \frac{1}{|\mathcal{E}|}\sum_{i=1}^{|\mathcal{E}|} \boldsymbol{I}_\mathrm{f}(\boldsymbol{e}_i). \quad (7)$$

  An ellipse representing the real catheter tip section should have high values in the filtered image $\boldsymbol{I}_\mathrm{f}$, thus this term needs to be maximized.
- The mean distance b_d of the points in $\mathcal{G}$ to $\mathcal{E}$:

$$b_\mathrm{d} = \frac{1}{|\mathcal{G}|}\sum_{i=1}^{|\mathcal{G}|} \min_j \|\boldsymbol{p}_i - \boldsymbol{e}_j\|_2. \quad (8)$$

  This feature measures how elliptical the point sequence $\mathcal{G}$ is.
- The coverage b_c of the ellipse by the points in $\mathcal{G}$ is given by

$$b_\mathrm{c} = \frac{\#\{\boldsymbol{e}_i \mid \min_j \|\boldsymbol{p}_j - \boldsymbol{e}_i\|_2 < \varepsilon\}}{|\mathcal{E}|}. \quad (9)$$

  This feature denotes what fraction of the ellipse is covered by the point sequence $\mathcal{G}$. A pixel of the ellipse is considered as covered if the distance to the next pixel of $\mathcal{G}$ is within ε.
- A feature with respect to the circumference of the ellipse is defined as

$$b_\mathrm{l} = \max(\Pi - |\mathcal{E}|, 0). \quad (10)$$

  The values of this feature should be low as its intention is to penalize ellipses that are smaller than Π. Very small ellipses rarely represent the catheter tip section but can have extraordinary good values for the coverage and the filter value, e.g. due to small bright spots in the filtered image. The length penalty reduces this bias towards small ellipses. The choice of Π depends on the expected image quality and ε.
- Angular difference b_a between shaft and tip candidate

$$b_a = |\phi_\mathrm{s} - \phi_\mathrm{t} - 180°|. \quad (11)$$

  Shaft and tip section start from the seed point with a start angle ϕ_s and ϕ_t, respectively. As they continue in different directions, the angular difference should approximate $180°$. This feature is used to define the direction of the catheter tip section if a clockwise or a counter clockwise direction are both possible.

Additionally there are some features that are used to reject candidates for which the ellipse is not plausible with respect to the known catheter shape.

- Length b_M and b_m of the major axis and minor axis, respectively. The maximum diameter of a currently available Lasso® catheter (Biosense Webster, Diamond Bar, CA, USA) is 25 mm. Given a projective magnification factor of less than 1.5 and a pixel spacing of 0,183 mm, the diameter of a CM catheter in the image is less than 205 pixel. Using this prior knowledge, candidates can be rejected if $b_\mathrm{M} > 220$ pixel. A candidate is also rejected if $b_\mathrm{m} < 20$ pixel. If the ellipse is degenerated and just a line, the catheter tip section cannot be detected by the current approach. Also the 3-D reconstruction will not work. In this cases the approach of Brost [32], [33] could be used.

The objective function that evaluates a path $\mathcal{G}$ and its associated ellipse $\mathcal{E}(\mathcal{G})$ is given by

$$b(\mathcal{G}, \mathcal{E}) = -\beta_\mathrm{fe} \cdot b_\mathrm{fe} - \beta_\mathrm{c} \cdot b_\mathrm{c} + \beta_\mathrm{d} \cdot b_\mathrm{d} + \beta_\mathrm{l} \cdot b_\mathrm{l} + \beta_\mathrm{a} \cdot b_\mathrm{a} \quad (12)$$

and needs to be minimized. The weights of features that need to be maximized have therefore a negative sign.

The number of possible tip section candidates may get very large. This depends on the complexity of the graph which is related to the image quality. Therefore, a population based method is used to find the best path [34]. The initial population consists of all possible paths of the search graph which start from the seed point and have a length of 100 pixels. In each iteration, all paths in one generation are evaluated. Then the next generation is computed by increasing the length of the previous generation by 30 pixel. If there is a bifurcation during those 30 pixels, the individual splits up and each new individual follows a different path. No individual may visit a path twice or a path that was already used for the shaft search. An exception is made for short segments which may

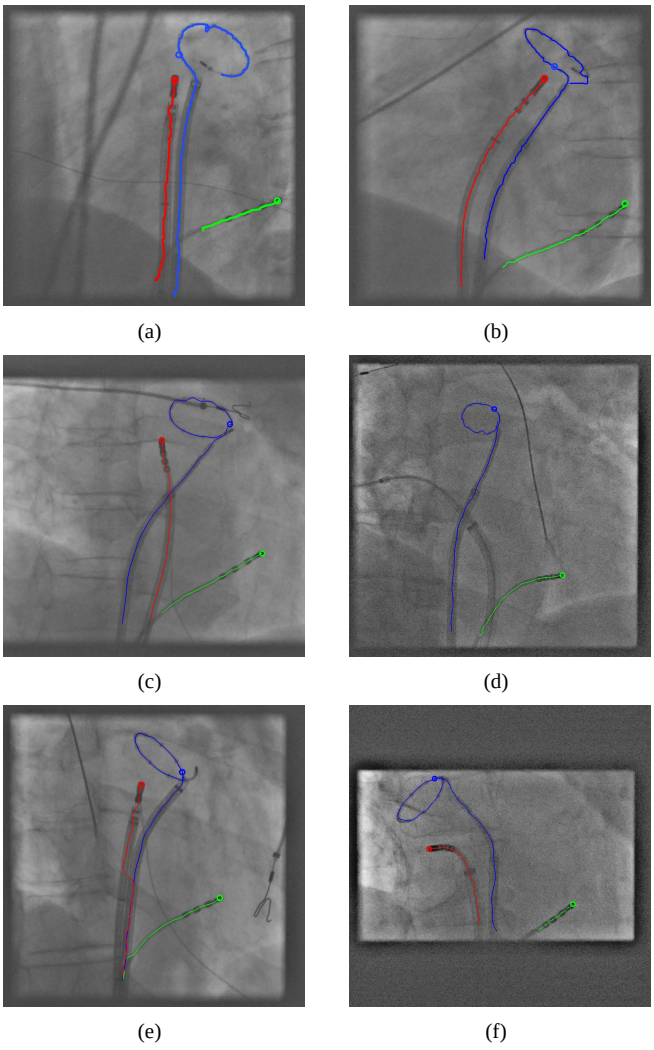

Fig. 6. Typical results of the catheter detection. Each catheter was detected separately. The seed points used for detection are marked with a circle and are placed at the tip of the linear catheters. For the CM catheter, the seed point was placed after the transition from the shaft to the tip.

be used twice to allow for self-crossings of the path. Only individuals with an objective value close to the best solution found so far will stay in the population. The optimization is terminated if no better solution was found three times in a row after the 10th generation or a length of 600 pixels is reached. This corresponds to a 25-mm Lasso® catheter tip.

D. 3-D Catheter Reconstruction

As last step, the catheter is reconstructed in 3-D using two images acquired under different views, e.g., using plane A and plane B of a biplane system. The result of the catheter detection for each image is given as a parametric 2-D curve, $C_{\mathrm{A}}(t_{\mathrm{A}})$ and $C_{\mathrm{B}}(t_{\mathrm{B}})$, $t_{\mathrm{A}}, t_{\mathrm{B}} \in [0,1]$, usually provided as cubic spline curves. Since we use a calibrated C-arm system with known projection matrices, candidates for point correspondences are identified using epipolar geometry, We then search for a maximum sequence of n point correspondences $((C_{\mathrm{A}}(t_{\mathrm{A},1}), C_{\mathrm{B}}(t_{\mathrm{B},1})), \ldots, (C_{\mathrm{A}}(t_{\mathrm{A},n}), C_{\mathrm{B}}(t_{\mathrm{B},n})))$ among the candidates such that their curve parameters $t_{\mathrm{A},1}, \ldots, t_{\mathrm{A},n}$ and $t_{\mathrm{B},1}, \ldots, t_{\mathrm{B},n}$ are placed in ascending order. The reconstruction algorithm is an improved version of a method by Baert *et al.* [21]. A detailed description can be found in [24] using a shortest-path-problem formulation or in [25], which uses a recursive formulation to solve this problem.

TABLE I
CLINICAL DATA USED FOR EVALUATION

Catheter	Number of biplane image pairs	Number of patients
RF	47	27
CS	61	47
CM	58	45
all	88	59

III. EVALUATION AND RESULTS

For the evaluation of the proposed catheter detection method and reconstruction algorithm, we used both clinical data and data from phantom experiments. Although clinical data reflects reality better, we could not use it to assess 3-D accuracy due to the lack of associated 3-D ground truth. Instead, 2-D catheter center lines in the images were extracted manually to obtain 2-D ground truth. To still provide insights into the 3-D reconstruction accuracy, we carried out a phantom study involving tomographic reconstruction using C-arm CT. We obtained 3-D ground truth using manual segmentation of catheter center lines in the C-arm CT volume. Two-dimensional ground truth was generated as for clinical data.

We carried out three types of evaluation: First, we performed catheter detection on clinical data and compared the result to our 2-D ground truth. We did not evaluate 2-D catheter detection on data acquired during the phantom study as these results have less clinical relevance. Second, we focused on inaccuracies related to our 3-D reconstruction method. As no 3-D ground truth was available for clinical data, we performed this error analysis on phantom experiment data. We used 2-D ground truth center lines as input for 3-D reconstruction to assess the reconstruction error independent of possible detection errors. The results were compared to the 3-D ground truth. Third, we combined our detection and 3-D reconstruction approach to estimate how detection inaccuracies affect the reconstruction result (combined approach). For clinical data, 3-D reference data was generated from 2-D ground truth center lines using our reconstruction method. Note that this reference data is subject to the 3-D reconstruction inaccuracies studied in the phantom experiment. Finally, the combined approach was also applied to phantom data. Although the results have less clinical significance, they are still valuable since the 3-D ground truth was not affected by any detection and triangulation errors as it had been obtained from 3-D tomographic C-arm CT data.

A. Experimental Setup and Data

The phantom study was performed on a C-arm biplane system (Artis zee biplane, Siemens AG, Healthcare Sector, Forchheim, Germany). Our experimental setup comprised a circular mapping (CM) catheter, a coronary sinus (CS) catheter

TABLE II
PARAMETER VALUES DETERMINED HEURISTICALLY FOR DETECTION

Description	Symbol	Value	Appears in
Reduced search space size	$\lvert\mathcal{S}_\mathrm{r}\rvert$	150,000	Sec. II-A
Closeness gain weighting	λ	1.25	Eq. 1
Cost reduction range width	ϱ	7 pixels	Eq. 2
Minimal circle length	l_c	75 pixels	Sec. II-B
Circle-gap-ratio	$l_\mathrm{c}/l_\mathrm{b}$	10	Sec. II-B
Ellipse coverage buffer	ε	10 pixels	Eq. 9
Small ellipse penalty	Π	200	Eq. 10

and a radio-frequency (RF) ablation catheter all inserted into a thorax phantom. Images were taken from different primary angles (RAO/LAO) and a static secondary angle (Cran/Caud) of $0°$. The angular difference was always $90°$ as this is currently clinical practice [35]. The primary angle ranged from -120° to -20° for plane A and from -30° to 70° for plane B. The step width was $10°$ resulting in 11 Biplane pairs All images show the CM, the CS and the RF catheter. For the catheters in these images, the 3-D ground truth position was extracted manually from a C-arm CT volume (*syngo* DynaCT, Siemens AG, Healthcare Sector, Forchheim, Germany).

The clinical data was made up of 88 biplane sequences (176 monoplane sequences) from 59 patients. Only the first frame of each sequence was taken as the image content did not change much throughout the sequence. From these images, not all could be used for every catheter type as not all catheters were always present. We also excluded biplane images for the CS catheter evaluation if the catheter was only visible at the lower border or very short. Furthermore, biplanes images where the CM catheter loop was degenerated to a line were not used for CM catheter evaluation. An overview of the number of remaining images and the number of patients they are associated with is given in TABLE I.

The clinical images were recorded during standard catheter ablation procedures performed at three clinical site on a C-arm biplane system (Artis zee biplane, Siemens AG, Healthcare Sector, Forchheim, Germany). The catheter center lines were manually extracted and then verified by a board-certified electrophysiologist. These center lines were later on used as ground truth for the retrospective evaluation.

To assess the spatial accuracy of our detected catheters, we obtained the mean and maximum error by sampling points along the detected catheters and computing the average and maximum of their distance to the associated ground truth. Furthermore, we calculated the coupling distance [26] normalized by the catheter length. This measure computes a point-wise mapping from one line to the other first. Then, it sums up the distances between these mappings. It is a symmetric measure and takes both wrongly detected catheter parts and undetected catheter parts into account.

The computations were performed on an Intel Core i7 2.6 Ghz CPU with 8 GB RAM and a Nvidia Quadro K1000M GPU. The GPU was used to generate the medialness image and the skeleton image.

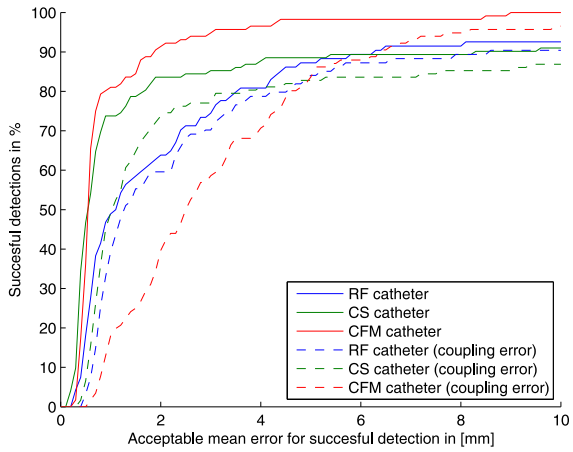

(a)

(b)

Fig. 7. (a) Success curve for catheter detection, both using the average distance to the manual ground truth annotation and the stricter coupling error. (b) Distribution of the maximum distance to the ground truth annotation in each image.

B. Detection Performance

To evaluate detection accuracy, parameter values depending on the image size, intensity quantification and spatial resolution were set heuristically. The values are provided in TABLE II. The pixel spacing was between 0.173 mm and 0.183 mm for all images. If a different pixel spacing is to be used, the parameters Π and l_c should be adapted accordingly. The various parameters α of the objection function for the shaft, Eq. (6), and the different weights β of the objective function for the catheter tip search, Eq. (12), were determined in a training step. Training of the detection parameters and evaluation was carried out in a leave-one-patient-out crossvalidation. That is, for the evaluation of one image, parameter training was carried out using all other datasets excluding the images that belonged to the currently evaluated patient. The parameters α_l and β_fe were set to a fixed value of 1 without loss of generality. The shaft parameters were trained separately for each catheter type, again, in a leave-one-patient-out cross-validation. The catheter tip section parameters for the CM catheter were obtained the same way. The optimization of the parameters was performed using grid search. For each parameter, a normalization factor was determined such that the expected maximum value is equal to 1. In the grid search, the weights ranged from 0 to this normalization factor. For each sequence, the seed point was manually set after the transition from the shaft to the tip section at the CM catheters as shown in Fig. 6. For the other catheter types, it was set at the top of the catheter tip. This seed point was fixed during the training

TABLE III
CATHETER DETECTION RESULTS.

Cathe-ter type	All detections: Mean dist. to reference ± std dev.	All detections: Mean coupling distance ± std dev.	All detections: False negative / false positive rate	All detections: Success rate	Successful detections: Mean dist. to reference ± std dev.	Successful detections: Mean coupling distance ± std dev.	Successful detections: False negative / false positive rate
RF	3.1 ± 5.5 mm	3.9 ± 7.0 mm	31.1 % / 27.5 %	84.0 %	1.3 ± 1.1 mm	1.6 ± 1.2 mm	21.2 % / 17.7 %
CS	2.9 ± 7.5 mm	5.6 ± 12.1 mm	25.2 % / 16.4 %	82.8 %	0.7 ± 0.7 mm	1.2 ± 0.8 mm	13.7 % / 6.8 %
CM	0.9 ± 1.3 mm	3.3 ± 3.0 mm	18.5 % / 7.8 %	83.6 %	0.6 ± 0.5 mm	2.3 ± 1.3 mm	14.0 % / 4.3 %
all	2.3 ± 5.6 mm	4.3 ± 8.4 mm	24.5 % / 16.6 %	83.4 %	0.9 ± 0.8 mm	1.7 ± 1.2 mm	15.9 % / 9.0 %

process and was also used for the evaluation.

We rated catheter detection a failure, if the average error was above 5.0 mm. A pixel was considered a false positive, if it was more than 2.0 mm away from the ground truth. The false negative rate was the percentage of the ground truth pixels which had no detected pixel within a 2.0 mm radius. An example of a successful detection result is shown in Fig. 6. A curve showing the success rate with respect to different error thresholds as well as the distribution of the maximum deviation from the ground truth annotation is given in Fig. 7. Detailed results are presented in TABLE III for all catheters.

To evaluate the sensitivity of the detection method with respect to different seed point placements, we evaluated the intra-user variability and the inter-user variability of the method. This evaluation was not performed for each of the 332 catheters, but we considered a representative subset of 20 images for each catheter type including images with a low and a high detection error as well as images with failed detections. For assessing the intra-user variability we used detection results coming from three different seed points of the same person. For the RF and the CS catheter, the variance in the coupling error was 0.1 mm or less. For the CM catheter, the variance was 0.5 mm. To assess the inter-user variability, we used detection results coming from three seed points marked by different persons. For the RF and the CS catheter, the variance in the coupling error was again 0.1 mm or less. For the CM catheter, the resulting coupling error had a variance of 0.6 mm.

The runtime for a single image was 2.8 s ± 3.6 s for the catheter detection with tip section search and 1.1 s ± 0.2 s if no tip search was used. The runtime doubles when catheters in both images of a biplane pair need to be detected, e.g. for 3-D reconstruction.

C. Reconstruction Performance

Three-dimensional reconstruction performance could only be evaluated for the phantom experiments. The ground truth catheter center lines in the biplane sequences were used as input for 3-D reconstruction. The result was then compared to the 3-D ground truth catheter positions derived from the C-arm CT. The mean error was 0.8 mm ± 0.3 mm for the RF ablation catheter, 0.7 mm ± 0.2 mm for the CS catheter and 1.0 mm ± 0.2 mm for the circular mapping catheter, respectively. Unfortunately, the same 3-D information of the catheters cannot be obtained in a clinical setup, since it is not possible to perform a C-arm CT for each biplane fluoroscopy scene. This is why an evaluation of the reconstruction accuracy on clinical data was not possible. The median runtime of the reconstruction was 32 ms.

D. Combined Detection and Reconstruction Performance

We also evaluated a combination of detection and reconstruction (combined approach). To this end, an automatic detection was performed on the catheters first. These detection results were then directly fed into the reconstruction algorithm. Since our goal was to investigate the overall accuracy when detection was successful, failed detections were not considered for evaluation of the combined approach. A detection was considered as failed if the mean distance to the ground truth was larger than 5.0 mm. From the phantom study data, three biplane pairs were not used for RF catheter evaluation, and two image pairs were not used for CS catheter evaluation due to misdetection. Misdetections happened e.g. because the CS catheter tip section in certain angulations was so close to the RF catheter that the RF catheter was detected instead of the CS catheter. For the CM catheter, five pairs could not be used as the tip section appeared as a line rather than as a loop. For the angulations with 90 degrees difference, the resulting mean 3-D coupling distance was 1.8 mm ± 1.1 mm. Broken down by catheter types, the error was 1.7 mm ± 0.8 mm for the RF catheter, 1.0 mm ± 0.3 mm for the CS catheter and 3.1 mm ± 1.2 mm for the CM catheter, respectively.

With clinical data, a combined approach was performed as well. As no 3-D ground truth information was available, 3-D catheter reconstruction based on 2-D ground truth center lines was used as reference. The computed differences can therefore only be considered as an estimation of the actual 3-D error. We found a mean coupling error of 2.2 mm ± 2.2 mm. In particular, the error was 1.7 mm ± 1.0 mm for the RF catheter, 1.8 mm ± 3.2 mm for the CS catheter and 3.1 mm ± 1.1 mm for the CM catheter. The coupling error is largely influenced by undetected catheter parts. To evaluate the accuracy of the actually reconstructed parts, we also calculated their distance to the ground truth. The overall mean displacement was 1.4 mm ± 1.7 mm. The error was 1.5 mm ± 1.0 mm for the RF catheter, 1.4 mm ± 2.5 mm for the CS catheter and 1.5 mm ± 0.8 mm for the CM catheter. A distribution of the displacement is given in Fig. 8.

IV. DISCUSSION

Overall, the results demonstrate that our approach is suitable for detection and reconstruction of catheters using only a single click per catheter in each image of a biplane image

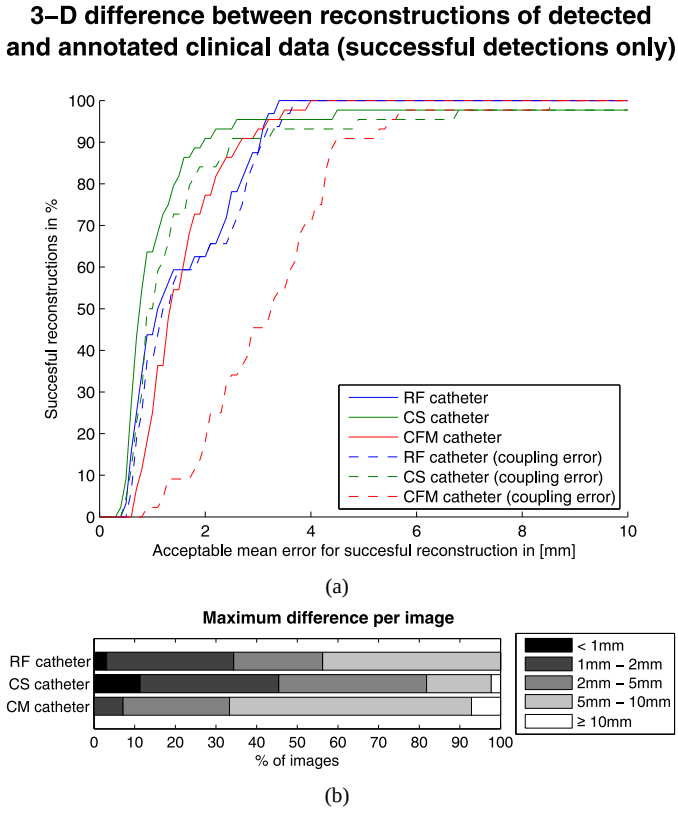

Fig. 8. (a) Success curve for catheter parts reconstructed by the combined approach. The error was computed with respect to a reconstruction result based on manual ground truth annotation of the clinical data. The overall mean displacement to the reference was $1.5\,\text{mm} \pm 1.0\,\text{mm}$ for the RF catheter, $1.4\,\text{mm} \pm 2.5\,\text{mm}$ for the CS catheter and $1.5\,\text{mm} \pm 0.8\,\text{mm}$ for the CM catheter. (b) Distribution of the maximum displacement in each image.

pair. However, there are some issues that need to be discussed in more detail.

A. Detection

The presented detection algorithm extends the previous approach [24] to more catheter types. The feature weights were according to the catheter type using a learning-based approach to make sure that this method generalizes well for unseen data. For the CS catheter, e.g., the most important feature was the length. The training yielded especially for the direction feature a lower weight compared to the other catheters. This corresponds to the often horizontal positioning of the CS catheter which is related to the coronary sinus anatomy. The RF catheter and the CM catheter, on the other hand, received higher weights for the curvature and the direction feature from training. These weights were nearly equal for both catheters as they are placed at similar positions inside the left atrium. Overall, the dedicated end-angle feature played a minor role as a correct catheter end at the bottom was also ensured by the curvature and direction features.

In our previous approach [24], we used heuristically determined feature weights to search for the CM catheter. Compared to the previous approach, we achieved different, in fact, slightly worse results which. We, however, consider them as more representative as the method was evaluated on a broader set of clinical images.

If the detection was successful, which was the case for over 82 % of the images, the mean coupling error was below 2 mm making this approach suitable for clinical use [36]. In case of an unsuccessful detection, often a wrong catheter was selected. In such a case, the resulting error could exceed 10 mm. For a failure, there are two main reasons: First, the contrast of the catheter may be poor resulting in a gap of the segmentation $\boldsymbol{I}_\text{b}$ that is too large. This can happen, for example, between the first and second RF catheter electrode and for some types of CS catheter. If the catheter overlaps with the dark diaphragm, catheter detection may also suffer. A combination with an electrode detection algorithm [12], [10], [37] could improve results. The second reason for detection failures are intersections of catheters with other structures such as ECG-leads. In many cases, these intersections are handled correctly as selecting the correct catheter segments minimizes the curvature. Nevertheless, in combination with poor contrast or if the catheter tip is close to a different catheter, see Fig. 9, the wrong catheter might be selected. We also investigated if the curvature of the catheter had an impact on the detection error, but we found no correlation.

The detection method has a low intra- and inter-user variability for the RF and the CS catheter. One reason for this is because, the position where the seed point should be placed is very distinct. In addition, as part of the initialization step, the seed point is moved to the closest skeleton point. As a consequence, the same skeleton point may be selected although different points in the image were chosen. For the CM catheter, the variability was higher as the point to be marked by the user is more ambiguous. Here, significantly different results may be computed if the wrong catheter direction was assumed or if the seed point was not placed after to the position where the circular tip starts but rather shortly before the position where the circular tip meets the shaft again.

Compared to a previously published method [14], which performs also a graph-based search using two or more points marked by the user, our method requires only one point. The false positive rate of 17.8 % reported by the authors of this publication is in the range of our method, except for the RF catheter. Their missing detection rate is about 17.6 %, which is better than our one-click per catheter method. However, the validity of a comparison based on these numbers is limited as the evaluation was not only performed on a different data set, but also on guide wires instead of EP catheters.

A more sophisticated catheter detection approach that searches simultaneously for all visible catheters could, however, take such crossings into account and avoid these problems. Also, adding a second seed point at the bottom of the catheter can be advantageous to detect the whole catheter. By selecting the catheter manually, the physician can ensure that the same catheter is detected in both images. If the catheter detection and reconstruction turns out to be successful and accepted in a clinical environment, user interaction could be reduced by catheter tip detection methods to determine the seed point automatically [38], [10], [11].

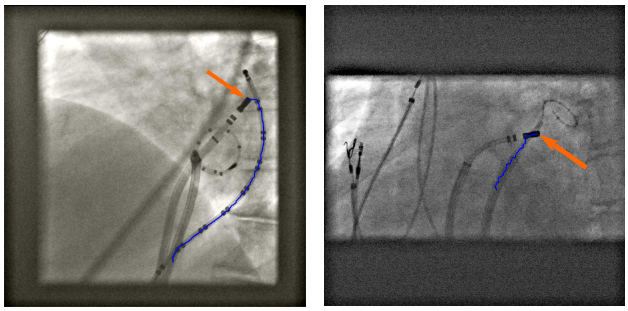

Fig. 9. Examples for misdetections. Both in (a) and in (b) the seed point was set at the top of the RF catheter pointed to by the arrow. Since the part between the first and the second electrode is not visible in the fluoroscopic image, the algorithm considers the tip as belonging to the CS catheter in (a) and to the CM catheter in (b), respectively.

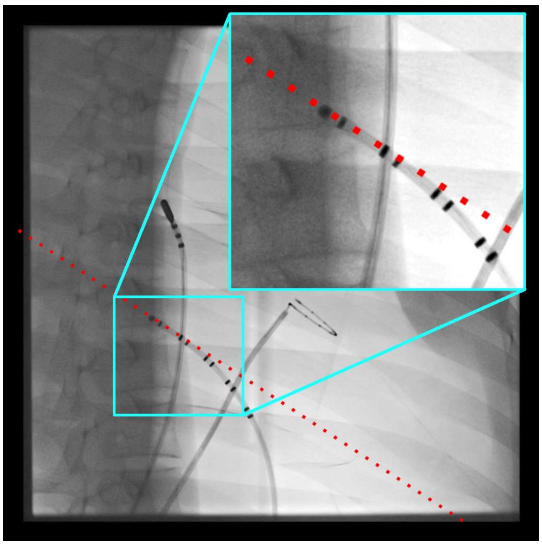

Fig. 10. Epipolar line for the CS catheter tip. The epipolar line is nearly parallel to the end of the catheter. Computing intersections with the centerline of the catheter and the epipolar line is therefore numerically unstable.

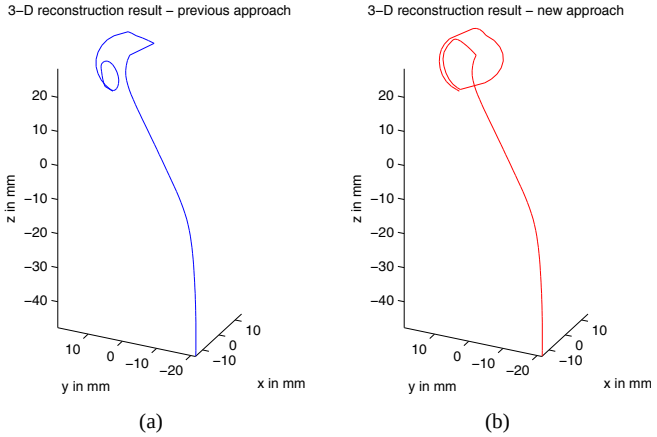

Fig. 11. Reconstruction result using a re-implementation of the previously suggested approach by Baert *et al.* (a) and our proposed method (b). While both methods perform well for the catheter shaft, the previous approach fails for the curved catheter tip section.

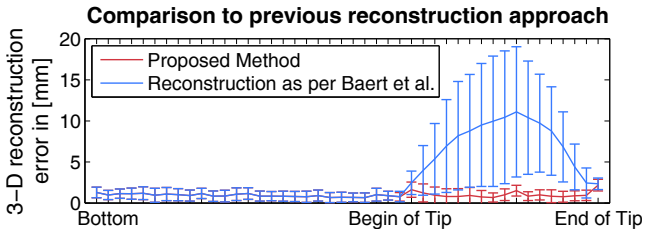

Fig. 12. The CM catheter of the phantom was reconstructed from the manual annotations of all pairwise combinations of the acquired images. The distance of the reconstructions to each point of the ground-truth annotation is plotted for a re-implementation of the method of Baert *et al.* (blue) and our proposed method (red). For the catheter shaft, the new method is equal to the previous approach. For the curved catheter tip section, the method of Baert *et al.* fails while the new proposed method is able to deal with this curved structure.

B. Reconstruction

We found that our proposed reconstruction method dealt better with curved catheters than the previously suggested approach by Baert *et al.* [21]. An example for the different reconstruction results is presented in Fig. 11. Also a quantitative evaluation comparing both approaches was carried out: For all possible pairs of 2-D images from the phantom study data, a reconstruction was computed using both approaches. The mean distance from the ground-truth data to the reconstruction results is given in Fig. 12. It shows that the approach by Baert *et al.* can deal well with small-curvature objects. But without the proposed search for point correspondences, a reconstruction of more strongly curved structures fails. However, some remaining limitations became apparent in the evaluation. They are discussed below.

The phantom study revealed a mean 3-D reconstruction error of up to 1.0 mm for a 90 degree angular difference between the two views. There are several possible sources for errors. First, the manually annotated ground truth center lines of the catheters, both in the 2-D fluoroscopic images and in the 3-D C-arm CT volume, may contain small errors. We also noticed that the error for the CM catheter was highest. High errors appear if for some parts of the catheter no point correspondences can be found. This can be the case when the epipolar line does not precisely intersect the catheter, e.g., due to small inaccuracies when estimating the biplane projection geometry. This can occur especially at points where the catheter is tangent to the epipolar line, see Fig. 10. As the CM catheter has a circular part, it is more prone to this kind of error. In such a case, the missing points are interpolated. The difficulty to find the right point correspondences if the catheter is tangential to the epipolar line is the major limitation of the reconstruction algorithm. However, this is a general problem that also affects manual reconstruction by triangulation.

The overall reconstruction results showed similar 3-D reconstruction errors as observed when triangulating a single point [39]. Also the dependency on the angle between the two viewing directions was found to be similar.

C. Combined Detection and Reconstruction

The combined approach using clinical data showed a correlation between detection quality and accuracy of the 3-D reconstruction. As no 3-D ground-truth was available, 3-D

reconstruction based on 2-D ground-truth data was used as reference. The error was measured using the coupling distance between this reference and the result of a combined detection and reconstruction. As a consequence, both inaccurate as well as missing parts in the 3-D reconstruction result contributed to this error. If the detection succeeded, the error was found to be $1.7\,\text{mm} \pm 1.0$ mm for the RF catheter and $1.8\,\text{mm} \pm 3.2$ mm for the CS catheter. A 2.0 mm error is considered acceptable from a clinical point of view [36]. For the CM catheter, the average coupling distance was $3.1\,\text{mm} \pm 1.1\,\text{mm}$. This is because the tip section of the CM catheter forms a circular structure which sometimes overlaps at the end. The overlapping part was included in the ground-truth annotation but it was often not detected and therefore missing in the 3-D reconstruction result, thus, leading to a higher coupling error. Considering only the actually reconstructed parts, the error reduced to $1.5\,\text{mm} \pm 0.8\,\text{mm}$.

The evaluation using data of our phantom study yielded notably lower errors for the RF catheter and the CS catheter. This is likely due to the detection step, as the phantom contained fewer additional structure such as ECG leads which can lead to small detection errors. However, for some images, the detection failed as the tip of one catheter was close to another catheter. For the CM catheter, the error was comparable to the clinical data as also here, the overlapping parts of the tip section were not always reconstructed.

The overall runtime of combined detection and reconstruction is about 2 s for the CS and the RF catheter. This facilitates computing a 3-D shape of the CS catheter for initial registration or as a registration reference throughout the case [40]. Real-time performance is not needed as this step, as this registration is only performed a few times during the procedure (possibly only once). Due to the run-time requirements and the user interactions involved, our method as currently implemented is not yet suited for continuous 3-D modelling. In these case, tracking methods can be used [20], [32]. However, our combined detection and reconstruction can be used to compute the initialization of the catheter required by these methods.

V. Conclusions

The results presented show that detection and reconstruction of a complete EP catheter is possible if only a single seed point per image is provided. The semi-automatic detection can be adapted to various EP catheters to take their different appearances into account. The detection and reconstruction error was in most cases below 2.0 mm, thus enabling catheter localization for clinical EP applications [36]. In some cases, e.g. when two catheters overlap, the wrong catheter may be detected. In these cases, manual correction may still be needed. Although the combined detection and reconstruction was affected by detection errors, it reached an accuracy of $1.0\,\text{mm} \pm 0.3\,\text{mm}$ to $3.1\,\text{mm} \pm 1.2\,\text{mm}$ depending on the catheter. These values are based on data collected during our phantom study. For clinical data, the respective average error of the combined approach was $1.8\,\text{mm} \pm 1.1\,\text{mm}$ to $3.1\,\text{mm} \pm 1.1\,\text{mm}$. Note that these numbers refer to the coupling distance [26]. We believe that the coupling distance is better suited for comparing curvilinear structures as it is also sensitive to undetected parts. Measuring simply the distance of detected parts to a reference, as applied in [21], [18] leads to a lower error of $1.4\,\text{mm} \pm 1.7\,\text{mm}$ to $1.5 \pm 1.0\,\text{mm}$ for the combined approach on clinical data depending on the catheter type.

Due to the small user interaction needed and high accuracy achievable, our method can be used for augmented fluoroscopy applications or as input for motion compensation algorithms in the context of EP procedures [41]. In fact, if a mechanical model of the RF catheter was available, then our a 3-D model may even be used to estimate contact force [6].

As the largest error of this approach are introduced in the detection step, an optional correction step should be provided in clinical practice. A workflow using our approach could be designed as follows: First, the assistant selects the type of catheter that should be reconstructed. Then, the seed point on the catheter is set in both images. After reconstruction, the 3-D shape of the catheter is shown, and the 2-D detection results, e.g. represented as spline curve, are overlaid on the fluoroscopic images. If severe detection errors are present, they can be corrected manually by moving or adding control points to the 2-D detection result. As detection and reconstruction are decoupled, the manually corrected 2-D shape of the catheter can be directly used to perform a new 3-D catheter reconstruction.

References

[1] H. Calkins, J. Brugada, D. Packer, R. Cappato, S. Chen, H. Crijns *et al.*, "HRS/EHRA/ECAS Expert Consensus Statement on Catheter and Surgical Ablation of Atrial Fibrillation: Recommendations for Personnel, Policy, Procedures and Follow-Up," *Europace*, vol. 9, no. 6, pp. 335 – 379, June 2007.

[2] F. H. M. Wittkampf, E. F. D. Wever, R. Derksen, A. A. M. Wilde, H. Ramanna, R. N. W. Hauer, and E. O. Robles de Medina, "LocaLisa: New Technique for Real-Time 3-Dimensional Localization of Regular Intracardiac Electrodes," *Circulation*, vol. 99, no. 10, pp. 1312–1317, March 1999.

[3] L. Gepstein, G. Hayam, and S. A. Ben-Haim, "A Novel Method for Nonfluoroscopic Catheter-Based Electroanatomical Mapping of the Heart: In Vitro and In Vivo Accuracy Results," *Circulation*, vol. 95, no. 6, pp. 1611–1622, March 1997.

[4] J. Ector, S. D. Buck, W. Huybrechts, D. Nuyens, S. Dymarkowski, J. Bogaert, F. Maes, and H. Heidbüchel, "Biplane three-dimensional augmented fluoroscopy as single navigation tool for ablation of atrial fibrillation: Accuracy and clinical value," *Heart Rhythm*, vol. 5, no. 7, pp. 957 – 964, July 2008.

[5] V. Y. Reddy, D. Shah, J. Kautzner, B. Schmidt, N. Saoudi, C. Herrera, P. Jaïs, G. Hindricks *et al.*, "The relationship between contact force and clinical outcome during radiofrequency catheter ablation of atrial fibrillation in the TOCCATA study," *Heart Rhythm*, vol. 9, no. 11, pp. 1789 – 1795, 2012.

[6] M. Khoshnam and R. Patel, "A pseudo-rigid-body 3R model for a steerable ablation catheter," in *2013 IEEE Int. Conf. Robotics and Automation (ICRA)*, Karlsruhe, Germany, May 2013, pp. 4427–4432.

[7] H.-J. Bender, R. Männer, C. Poliwoda, S. Roth, and M. Walz, "Reconstruction of 3D Catheter Paths from 2D X-ray Projections," in *Medical Image Computing and Computer-Assisted Intervention–MICCAI'99*, ser. LNCS, C. Taylor and A. Colchester, Eds., vol. 1679. Cambridge, UK: Springer Berlin Heidelberg, September 1999, pp. 981–989.

[8] E. Franken, P. Rongen, M. van Almsick, and B. ter Haar Romeny, "Detection of Electrophysiology Catheters in Noisy Fluoroscopy Images," in *Medical Image Computing and Computer-Assisted Intervention – MICCAI 2006*, ser. LNCS, R. Larsen, M. Nielsen, and J. Sporring, Eds., vol. 4191. Copenhagen, Denmark: Springer Berlin Heidelberg, October 2006, pp. 25–32.

[9] L. Yatziv, M. Chartouni, S. Datta, and G. Sapiro, "Toward Multiple Catheters Detection in Fluoroscopic Image Guided Interventions," *IEEE Trans. Inf. Technol. Biomed.*, vol. 16, no. 4, pp. 770 –781, July 2012.

[10] Y. Ma, N. Gogin, P. Cathier, R. J. Housden, G. Gijsbers, M. Cooklin, M. O'Neill, J. Gill, C. A. Rinaldi, R. Razavi, and K. S. Rhode, "Real-time x-ray fluoroscopy-based catheter detection and tracking for cardiac electrophysiology interventions," *Med. Phys.*, vol. 40, no. 7, pp. 071 902–1 – 071 902–13, July 2013.

[11] W. Wu *et al.*, "Learning-based Hypothesis Fusion for Robust Catheter Tracking in 2D X-ray Fluoroscopy," in *2011 IEEE Conf. Computer Vision and Pattern Recognition*. Provicence, RI, USA: IEEE, June 2011, pp. 1097–1104.

[12] M. Cazalas, V. Bismuth, and R. Vaillant, "An Image-Based Catheter Segmentation Algorithm for Optimized Electrophysiology Procedure Workflow," in *Functional Imaging and Modeling of the Heart*, ser. LNCS, S. Ourselin, D. Rueckert, and N. Smith, Eds., vol. 7945. London, UK: Springer Berlin Heidelberg, June 2013, pp. 182–190.

[13] F. Milletari, N. Navab, and P. Fallavollita, "Automatic Detection of Multiple and Overlapping EP Catheters in Fluoroscopic Sequences," in *Medical Image Computing and Computer-Assisted Intervention MICCAI 2013, Part III*, ser. LNCS, K. Mori, I. Sakuma, Y. Sato, C. Barillot, and N. Navab, Eds., vol. 8151. Nagoya, Japan: Springer Berlin Heidelberg, September 2013, pp. 371–379.

[14] P. Wang, W.-s. Liao, T. Chen, S. Zhou, and D. Comaniciu, "Graph based interactive detection of curve structures in 2d fluoroscopy," in *Medical Image Computing and Computer-Assisted Intervention MICCAI 2010*, ser. LNCS, T. Jiang, N. Navab, J. Pluim, and M. Viergever, Eds. Springer Berlin Heidelberg, 2010, vol. 6363, pp. 269–277.

[15] A. Barbu, V. Athitsos, B. Georgescu, S. Böhm, P. Durlak, and D. Comaniciu, "Hierarchical Learning of Curves Application to Guidewire Localization in Fluoroscopy," in *2007 IEEE Conf. on Computer Vision and Pattern Recognition*, Minneapolis, MN, USA, June 2007, pp. 1–8.

[16] V. Bismuth, R. Vaillant, H. Talbot, and L. Najman, "Curvilinear Structure Enhancement with the Polygonal Path Image - Application to Guide-Wire Segmentation in X-Ray Fluoroscopy," in *Medical Image Computing and Computer-Assisted Intervention MICCAI 2012, Part II*, ser. LNCS, N. Ayache, H. Delingette, P. Golland, and K. Mori, Eds., vol. 7511. Nice, France: Springer Berlin Heidelberg, October 2012, pp. 9–16.

[17] M. Spiegel, M. Pfister, D. Hahn, V. Daum, J. Hornegger, T. Struffert, and A. Dörfler, "Towards Real-time Guidewire Detection and Tracking in the Field of Neuroradiology," in *Medical Imaging 2009: Visualization, Image-Guided Proceudres, and Modeling*, ser. Proc. of SPIE, M. Miga and K. Wong, Eds., vol. 7261, Lake Buena Vista, FL, USA, February 2009, pp. 726 105–1 – 726 105–8.

[18] P. Wang, T. Chen, Y. Zhu, W. Zhang, S. K. Zhou, and D. Comaniciu, "Robust guidewire tracking in fluoroscopy," in *2009 IEEE Conf. on Computer Vision and Pattern Recognition (CVPR 2009)*. Maimi, FL, USA: IEEE, June 2009, pp. 691–698.

[19] C. Cañero, F. Vilarino, J. Mauri, and P. Radeva, "Predictive (Un)distortion Model and 3-D Reconstruction by Biplane Snakes," *IEEE Trans. Med. Imag.*, vol. 21, no. 9, pp. 1188–1201, September 2002.

[20] M. Schenderlein, S. Stierlin, R. Manzke, V. Rasche, and K. Dietmayer, "Catheter Tracking in Asynchronous Biplane Fluoroscopy Images by 3D B-Snakes," in *Medical Imaging 2010: Visualization, Image-Guided Proceudres, and Modeling*, ser. Proc. of SPIE, K. Wong and M. Miga, Eds., vol. 7625, San Diego, CA, USA, February 2010, pp. 76 251U–1 – 76 251U–9.

[21] S. A. M. Baert, E. B. van de Kraats, T. van Walsum, M. A. Viergever, and W. J. Niessen, "Three-Dimensional Guide-Wire Reconstruction From Biplane Image Sequences for Integrated Display in 3-D Vasculature," *IEEE Trans. Med. Imag.*, vol. 22, no. 10, pp. 1252–1258, October 2003.

[22] A. Brost, R. Liao, N. Strobel, and J. Hornegger, "Respiratory motion compensation by model-based catheter tracking during EP procedures," *Med. Image Anal.*, vol. 14, no. 5, pp. 695–706, October 2010, special Issue on the 12th International Conference on Medical Image Computing and Computer-Assisted Intervention (MICCAI) 2009.

[23] S. Ernst, J. K. Chun, A. Ujeyl, F. Ouyang, and K.-H. Kuck, "sequential mapping mimicking simultaneous mapping using magnetic navigation during catheter ablation of supraventricular tachycardia: Results of the single dx study," *J. Cardiovasc. Electrophysiol.*, vol. 18, no. s1, pp. S11–S17, 2007.

[24] M. Hoffmann, A. Brost, C. Jakob, F. Bourier, M. Koch, K. Kurzidim, J. Hornegger, and N. Strobel, "Semi-Automatic Catheter Reconstruction from Two Views," in *Medical Image Computing and Computer-Assisted Intervention – MICCAI 2012, Part II*, ser. LNCS, N. Ayache, H. Delingette, P. Golland, and K. Mori, Eds., vol. 7511. Nice, France: Springer Berlin Heidelberg, October 2012, pp. 584–591.

[25] M. Hoffmann, A. Brost, C. Jakob, M. Koch, F. Bourier, K. Kurzidim, J. Hornegger, and N. Strobel, "Reconstruction method for curvilinear structures from two views," in *Medical Imaging 2013: Image-Guided Procedures, Robotic Interventions, and Modeling*, ser. Proc. of SPIE, D. R. Holmes and Z. R. Yaniv, Eds., vol. 8671, Lake Buena Vista, FL, USA, February 2013, pp. 86 712F–1 – 86 712F–8.

[26] T. Eiter and H. Mannila, "Computing Discrete Fréchet Distance," Technische Universität Wien, Tech. Rep., April 1994.

[27] M. Gülsün and H. Tek, "Robust Vessel Tree Modeling," in *Medical Image Computing and Computer-Assisted Intervention–MICCAI 2008, Part 1*, ser. LNCS, D. Metaxas, A. L., G. Fichtinger, and G. Szekely, Eds., vol. 5241. New York, NY, USA: Springer Berlin Heidelberg, September 2008, pp. 602–611.

[28] R. C. Gonzalez and R. E. Woods, *Digital Image Processing*, 3rd ed. Prentice Hall, 2008.

[29] J. M. Cychosz, *Graphics Gems IV*. Morgan Kaufmann, 1994, ch. Efficient Binary Image Thinning Using Neighborhood Maps, pp. 465–473.

[30] T. Cormen, C. Leiserson, and R. Rivest, *Introduction to algorithms*. MIT Press, 1990.

[31] P. Felzenszwalb and D. Huttenlocher, "Distance Transforms of Sampled Functions," Cornell University, Tech. Rep., September 2004.

[32] A. Brost, R. Liao, J. Hornegger, and N. Strobel, "3-D Respiratory Motion Compensation during EP Procedures by Image-Based 3-D Lasso Catheter Model Generation and Tracking," in *Medical Image Computing and Computer-Assisted Intervention–MICCAI 2009, Part I*, ser. LNCS, G.-Z. Yang, D. Hawkes, D. Rueckert, A. Noble, and C. Taylor, Eds., vol. 5761. London, UK: Springer Berlin Heidelberg, September 2009, pp. 394–401.

[33] ——, "3-D Model-Based Catheter Tracking for Motion Compensation in EP Procedures," in *Medical Imaging 2010: Visualization, Image-Guided Proceudres, and Modeling*, ser. Proc. of SPIE, K. Wong and M. Miga, Eds., vol. 7625, San Diego, CA, USA, February 2010, pp. 762 507–1 – 762 507–12.

[34] T. Bäck, U. Hammel, and H. Schwefel, "Evolutionary computation: Comments on the history and current state," *IEEE Trans. Evol. Comput.*, vol. 1, no. 1, pp. 3–17, 1997.

[35] M. Koch, M. Hoffmann, M. Pfister, J. Hornegger, and N. Strobel, "Optimized viewing angles for cardiac electrophysiology ablation procedures," *Int. J. Comput. Assisted Radiology and Surgery*, vol. 10, pp. 651–664, 2015.

[36] M. Esteghamatian, Z. Azimifar, P. Radau, and G. Wright, "Real-Time 2D-3D MR Cardiac Image Registration During Respiration Using Extended Kalman Filter Predictors," in *2008 9th Int. Conf. on Signal Processing*. Beijing, China: IEEE, October 2008, pp. 1325–1328.

[37] S. Kaeppler *et al.*, "Semi-automatic catheter model generation using biplane x-ray images," in *10th IEEE Int. Symp. on Biomedical Imag.* San Francisco, CA, USA: IEEE, April 2013, pp. 1416 – 1419.

[38] T. Kurzendorfer, A. Brost, C. Jakob, P. W. Mewes, F. Bourier, M. Koch, K. Kurzidim, J. Hornegger, and N. Strobel, "Cryo-Balloon Catheter Localization in Fluoroscopic Images," in *Medical Imaging 2013: Image-Guided Procedures, Robotic Interventions, and Modeling*, ser. Proc. of SPIE, D. R. Holmes and Z. R. Yaniv, Eds., vol. 8671, Lake Buena Vista, FL, USA, February 2013, pp. 86 710C–1 – 86 710C–8.

[39] A. Brost, N. Strobel, L. Yatziv, W. Gilson, B. Meyer, J. Hornegger, J. Lewin, and F. Wacker, "Accuracy of X-Ray Image-Based 3D Localization from Two C-Arm Views: A Comparison Between an Ideal System and a Real Device," in *Medical Imaging 2009: Visualization, Image-Guided Proceudres, and Modeling*, ser. Proc. of SPIE, M. Miga and K. Wong, Eds., vol. 7261, Lake Buena Vista, FL, USA, February 2009, pp. 72 611Z–1 – 72 611Z–10.

[40] A. Brost, F. Bourier, L. Yatziv, M. Koch, J. Hornegger, N. Strobel, and K. Kurzidim, "First steps towards initial registration for electrophysiology procedures," in *Medical Imaging 2011: Visualization, Image-Guided Procedures, and Modeling*, K. H. Wong and D. R. Holmes III, Eds., vol. 7964. Lake Buena Vista, FL, USA: SPIE, February 2011, pp. 79 641P–1 – 79 641P–8.

[41] A. Brost *et al.*, "Constrained Registration for Motion Compensation in Atrial Fibrillation Ablation Procedures," *IEEE Trans. Med. Imag.*, vol. 31, no. 4, pp. 870–881, April 2012.